JACS
JOURNAL OF THE AMERICAN CHEMICAL SOCIETY
pubs.acs.org/JACS
Article

Unlocking Multielectron Transfer in a Quinone−Pyrazine Conjoined Redox Core for Capacity-Doubled and Ultrastable Aqueous Organic Redox Flow Batteries

Pengbo Zhang, Yongkang Chen, Yuzhu Liu, Jie Wei, Zuoao Wu, Binze Yang, Guochun Ding, Sheng Wen, Tengfei Dai, Zhihu You, Zuoxiu Tie, Yichao Yan, and Zhong Jin*

Cite This: J. Am. Chem. Soc. 2025, 147, 46582−46593

Read Online

ACCESS | Metrics & More | Article Recommendations | Supporting Information

ABSTRACT: Aqueous organic redox flow batteries (AORFBs) face energy density and stability challenges. We introduce DAPQ, an anthraquinone−phenazine fused molecule with a π-conjugated architecture enabling four-electron storage. The rigid fused-ring structure integrates four redox-active sites, enhancing aromaticity to resist degradation while achieving reversible multielectron transfer and superior volumetric capacity. The 0.6 M DAPQ-based AORFB delivers an exceptionally high energy density of 53.59 Wh L^{-1} (53.48 Ah L^{-1}), and the 0.5 M DAPQ-based AORFB delivers a capacity retention of 99.86% over 2,300 cycles (1991 h), showing merely 0.0017% daily decay. Stable operation persists even at 50 °C, confirming conjugated rigidity's critical role in redox core stabilization and longevity. Mechanistic studies reveal that extended π-conjugation and balanced charge distribution synergistically inhibit parasitic reactions. This conjugation-driven multielectron design establishes a paradigm for developing high-capacity, durable organic charge carriers, advancing scalable, safe, and sustainable grid-scale energy storage solutions.

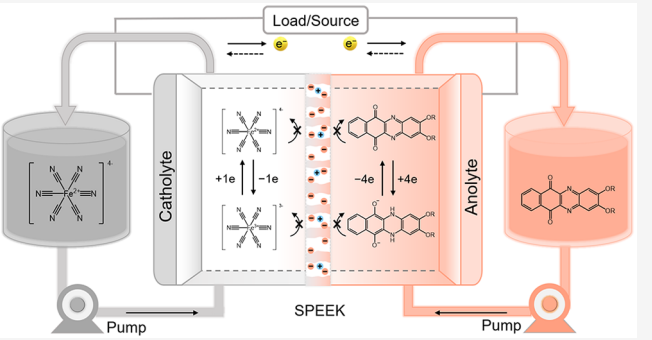

INTRODUCTION

Clean energy generation approaches, exemplified by solar and wind power, are imperative for realizing sustainable development and mitigating carbon emissions.[1,2] Nonetheless, their intermittent and distributed nature poses significant challenges to developing safe and cost-effective grid-scale energy storage technologies.[3,4] Aqueous redox flow batteries (ARFBs) stand out due to their highly modular and scalable design, allowing for straightforward scaling of electrolyte volume to achieve MW-level energy storage.[5,6] For example, all-vanadium redox flow batteries (AVRFBs) have been commercialized, utilizing different oxidation states of vanadium.[7,8] Nevertheless, the constrained vanadium resource contributes to high system costs, and issues such as low energy density and electrolyte cross-contamination persist. Therefore, exploring alternative redox-active species with abundant source, high energy density, and ultrastability is imperative.[9,10]

Renewable organic compounds, primarily composed of C, H, and O, have emerged as promising candidates to reduce dependency on rare minerals and enable large-scale, low-cost energy storage.[4,11,12] Moreover, the high versatility and tunability of organic compounds offer the potential to achieve a high capacity and long cycle lifespan. To date, various organic redox materials have been devised, including viologen,[13,14] ferrocene,[15] anthraquinone,[9,16] phenazine,[17,18] and their respective derivatives. At present, anthraquinone and phenazine derivatives are expected to be promising anode materials for aqueous organic redox flow batteries (AORFBs). However, anthraquinone derivatives tend to form electrochemically inactive dimeric anthrones upon cycling, while phenazine derivatives are prone to tautomeric changes, resulting in capacity fading.[18−20] Although grafting functional groups on the aromatic cores can enhance cyclic stability, the energy density is still not satisfying, posing a challenge for commercialization.[10,21,22] In general, organic active molecules with stronger aromaticity exhibit better redox stability. Additionally, incorporating multiple redox sites into active molecules can significantly increase charge storage density.[23] Hence, developing advanced organic structures that combine high energy density and robust stability is crucial for the development of AORFBs toward large-scale practical applications.

Received: October 10, 2025
Revised: November 19, 2025
Accepted: November 20, 2025
Published: December 4, 2025

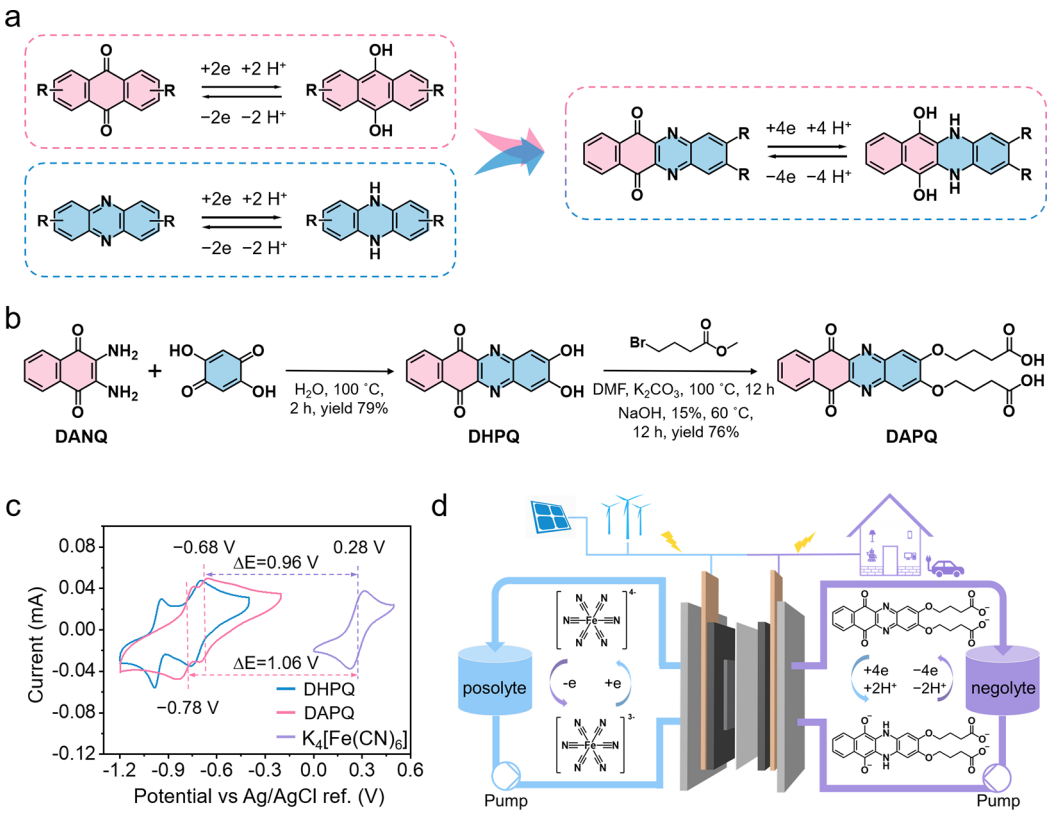

Figure 1. (a) Molecular design of DAPQ inspired by conjoining two representative redox-active organic compounds—anthraquinone and phenazine derivatives. (b) The synthesis route of the DHPQ intermediate and DAPQ final product. (c) CV curves of 2 mM DHPQ, DAPQ, and $K_4[Fe(CN)_6]$ dissolved in 1.0 M KOH solutions at a scan rate of 100 mV s^{-1}. (d) Structural configuration of the DAPQ||$K_4[Fe(CN)_6]$ AORFBs based on the DAPQ anolyte and $K_4[Fe(CN)_6]$ catholyte.

Herein, we propose a π-conjugation extension strategy to design and synthesize a water-soluble, quinone−pyrazine fused π-conjugation redox core, named 4,4'-((6,11-dioxo-6,11-dihydrobenzo[*b*]phenazine-2,3-diyl)bis(oxy))dibutanoic acid (DAPQ). This unique molecular structure demonstrates a doubling of energy density and significantly enhanced stability compared to single quinone or pyrazine derivatives. The DAPQ features a conjoined π-conjugation structure with four-electron transfer sites, facilitating efficient and reversible electron transfer across different redox states and enabling a higher energy density. Additionally, the extended and rigid π-conjugated fused-ring structure of DAPQ effectively mitigates structural degradation caused by potential nucleophilic attacks in solution, demonstrating excellent cycling stability at both room temperature and 50 °C. When paired with potassium ferrocyanide ($K_4[Fe(CN)_6]$) as the catholyte, the DAPQ-based AORFBs achieved an energy density of 53.59 Wh L^{-1} (53.48 Ah L^{-1}) at a concentration of 0.6 M. Remarkably, the 0.5 M DAPQ-based AORFBs retained 99.86% of its capacity after 1991 h (2300 cycles) of operation period, corresponding to an extremely low daily capacity decay rate of 0.0017%. To understand the redox mechanism and long-term stability of DAPQ, we employed a combination of nuclear magnetic resonance (NMR), in situ Fourier transform infrared (FTIR), in situ ultraviolet−visible (UV−vis) absorption spectroscopy, and electron paramagnetic resonance (EPR) and theoretical simulations. These studies reveal that the quinone−pyrazine conjoined redox core maintains a stable rigid ring structure during consecutive cycling, effectively preventing capacity fade caused by anthraquinone disproportionation and/or molecular isomerization. These findings underscore the effectiveness of conjoined molecule design and multiple charge storage in significantly enhancing both the energy density and long-term stability of AORFBs, paving the way for developing scalable, safe, and sustainable electrochemical energy storage systems.

RESULTS AND DISCUSSION

Generally, an ideal organic active molecule should demonstrate three critical attributes: (1) high aqueous solubility, (2) reversible multielectron transfer, and (3) structural stability. The design of DAPQ molecule, featuring multielectron storage capability and a π-conjugated fused-ring structure, was inspired by conjoining quinone and phenazine derivatives (Figure 1a). Previous efforts on the synthesis and modification of these derivatives have demonstrated prominent improvements in solubility and reversibility.[6,10,16−20,23−32] However, single-type quinone or phenazine molecules, primarily involving two-electron/two-proton transfer reactions, often struggle to simultaneously achieve a high capacity and long-term cycling life. To overcome these limitations, we optimized the molecular structure to integrate both quinone and phenazine redox cores. Although some fused structures have been reported in the context of nonaqueous organic energy storage, our design specifically considers the requirements of aqueous flow batteries.[33−35] In particular, through further optimization of the fused structure, additional sites for water-solubilizing side-group modification are provided, which enables the preparation of highly water-soluble, multielectron-storage DAPQ active molecules. These molecules exhibit an improved specific capacity compared to state-of-the-art single quinone or

https://doi.org/10.1021/jacs.5c17809
J. Am. Chem. Soc. 2025, 147, 46582−46593

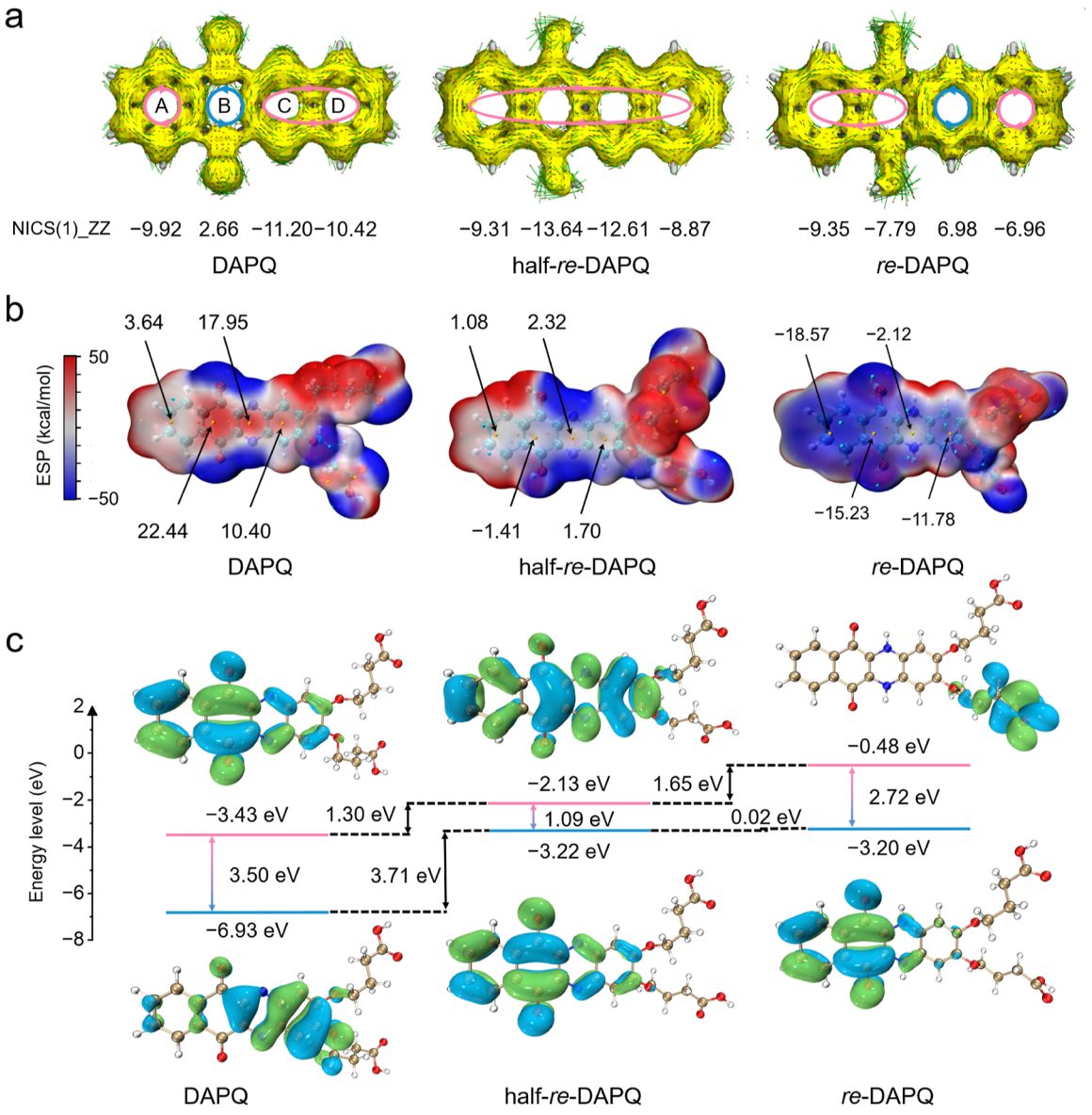

Figure 2. DFT investigation on the electronic structures of DAPQ, half-re-DAPQ, and re-DAPQ species. (a) Calculated NICS(1)_ZZ values and corresponding AICD plots of these species. The basal plane of the DAPQ unit is positioned perpendicular to the magnetic field vector. The small green arrows represent computed current density vectors, while the red or blue circles, labeled by arrows, indicate the global ring current flow direction. (b) Molecular ESP energy surfaces of these species. Only the corresponding values on the aromatic rings were labeled. (c) The molecular orbitals and energy gaps of these species at different redox states.

phenazine derivatives (Figure S1).[18,26,32] This enhancement translates into a higher energy density, lower material consumption, and reduced costs in large-scale energy storage systems, making DAPQ a promising and practical solution to the current limitations of AORFBs.

The schematic synthetic pathway of DAPQ in this work is illustrated in Figure 1b, in which a sequence of efficient synthetic steps was employed.[36−38] The detailed synthesis procedures are provided in the Supporting Information. Initially, the 2,3-diaminonaphthalene-1,4-dione (DANQ) precursor was produced by the amination of 2,3-dichloro-1,4-naphthoquinone through the Gabriel reaction. Subsequently, a Schiff base reaction was employed to condense DANQ with 2,5-dihydroxy-1,4-benzoquinone, yielding the 2,3-dihydroxybenzo[*b*]phenazine (DHPQ) intermediate. Then, methyl 4-bromobutyrate was grafted onto DHPQ, and the resulting compound was hydrolyzed to yield the DAPQ target molecule. The molecular structures and high purities of DANQ precursor, DHPQ intermediate, and DAPQ final product were confirmed via ^{1}H and ^{13}C NMR spectra (Figures S2−S7).

The aqueous solubility of both the DHPQ intermediate and DAPQ at pH 14 was assessed using UV−vis absorption spectroscopy (Figure S8). Notably, the DHPQ intermediate exhibited limited solubility (0.11 M), attributed to hydrogen bonding between the adjacent phenolic hydroxyl groups.[39] This low solubility negatively impacts the energy density and reduces the practicality in AORFBs. Based on both previous reports and our previous studies, alkoxy-substituted butyric acids bearing longer side chains can function as efficient solubilizing groups, since they not only enhance molecular stability but also improve tolerance to prolonged electrochemical reactions.[26,40,41] Following this thought, two *O*-butanoic acid side groups were grafted onto the DHPQ

https://doi.org/10.1021/jacs.5c17809
J. Am. Chem. Soc. 2025, 147, 46582−46593

intermediate, resulting in a highly water-soluble DAPQ compound. UV−vis absorption analysis revealed that DAPQ achieved a solubility of 0.61 M at pH 14, corresponding to an electron storage concentration of 2.44 M and a theoretical capacity of 65.39 Ah L^{-1}. These values surpass those of most existing quinone and phenazine derivatives,[42−44] positioning DAPQ as a promising candidate for the anolyte in AORFBs.

The electrochemical behaviors of the DHPQ intermediate and DAPQ in aqueous solutions at pH 14 were investigated by cyclic voltammetry (CV) (Figure 1c). Both compounds exhibited two pairs of reversible redox peaks. For DAPQ, the redox peaks appeared at −0.78 and −0.68 V, in comparison to those of the DHPQ intermediate at −0.96 and −0.73 V (vs Ag/AgCl). The first peak of DAPQ corresponds to the two-electron reduction of the quinone moieties. The second peak arises from a combination of the four-electron stepwise/consecutive reduction of unreacted DAPQ in solution and the two-electron reduction of semireduced DAPQ diffusing back to the electrode, giving a higher peak current. The decreased redox potential in DAPQ is attributed to the introduction of solubilizing groups, which disrupts the p−π conjugation of deprotonated phenolic hydroxyl groups under alkaline conditions. This disruption reduces electron delocalization and weakens their strong electron-donating effect, leading to a positive shift in redox potential relative to the DHPQ core. Moreover, in the ^{1}H NMR spectrum (Figure S9), the characteristic peaks in the aromatic region of DAPQ shift to higher values under alkaline conditions, indicating a reduction in the negative charge on its redox-active core. The two closely spaced redox peaks indicate that the redox-active sites of DHPQ couple effectively, enabling rapid electron transfer across the reduction and oxidation states. This suggests its superior reversibility as an anolyte in AORFBs. When paired with $K_4[Fe(CN)_6]$ as the catholyte, both DHPQ and DAPQ anolytes can achieve a full-cell voltage exceeding 1 V under pH 14. As a demonstration, DAPQ||$K_4[Fe(CN)_6]$ AORFBs based on DAPQ anolyte, $K_4[Fe(CN)_6]$ catholyte, and custom-made highly sulfonated polyetheretherketone (SPEEK) membrane separator were assembled and tested, as illustrated in Figure 1d.

The CV analyses of DAPQ at varying pH values were employed to construct the corresponding Pourbaix diagram, providing insights into the proton/electron transfer kinetics involved in its redox process (Figure S10). In the pH range above 11.89, the diagram shows two distinct linear regions with slopes of 4.1 mV pH^{-1} and 45.5 mV pH^{-1}, corresponding to the quinone and pyrazine units, respectively. In contrast, within the pH range 6.07−10.96, DAPQ exhibits a single merged peak with a slope of 10.4 mV pH^{-1}. These results indicate that under strongly alkaline conditions, the redox processes of DAPQ occur stepwise and consecutively: first, a two-electron, zero-proton step and then followed by a two-electron, two-proton step. In the weakly alkaline to near-neutral pH range, the process corresponds to a four-electron, single-proton transfer, and thus, only a single merged peak is observed because the change in pH brings the potentials of the two redox peaks closer together, resulting in a combined wave. Notably, the slopes slightly deviate from the theoretical values (0 mV pH^{-1}, 14.75 mV pH^{-1} and 59 mV pH^{-1}) predicted by the Nernst equation. This discrepancy is hypothesized to stem from the interactions between the quinone and pyrazine units during the redox processes, where their close π-conjugation and spatial proximity facilitate hydrogen bonding with water molecules at both redox sites, thereby subtly altering the local proton activity and leading to the observed deviation.

To investigate these interactions further, computational studies were conducted to quantify the mutual effects between the quinone and pyrazine units. Figure S11 illustrates the deprotonation tendencies of carbonyl groups in the half-reduced and fully reduced forms of DAPQ (i.e., half-re-DAPQ and re-DAPQ), revealing that the pyrazine moiety modulates the thermodynamics of carbonyl deprotonation through intramolecular hydrogen bonding. However, this interaction does not change the overall thermodynamic preference for complete deprotonation of the carbonyl groups. Figure S12 highlights the hydrogen-bonding interactions between DAPQ and water molecules across various reduction states, demonstrating that the adjacent quinone and pyrazine active units within the DAPQ molecule thermodynamically favor forming a stable chelated structure with a single water molecule. These findings imply that the electrode equilibrium reaction of DAPQ is influenced by the hydrogen-bonding interactions between its quinone and pyrazine units.

To investigate the electronic properties of DAPQ, in comparison to traditional anthraquinone or phenazine derivatives in different redox states, calculations of anisotropy of the induced current density (AICD) and nucleus-independent chemical shift (NICS) were conducted (Figures 2a and S13). NICS calculations, with negative values indicating aromaticity and positive values suggesting antiaromaticity, assessed the molecular aromaticity of unsubstituted anthraquinone, phenazine, and conjoined DAPQ core across various redox states. Specifically, NICS(1)_ZZ represents the negative magnetic shielding value measured 1 Å above the geometric center of the conjugated molecular plane, oriented perpendicular to the ring. This parameter is widely recognized and frequently used as a reliable criterion for assessing aromaticity.[45] In its pristine state, DAPQ exhibited significant aromaticity in rings A−D, while ring B showed weak antiaromaticity. In contrast, pristine anthraquinone exhibited strong antiaromaticity in ring F, and phenazine displayed pronounced aromaticity in ring I. These results demonstrate that the π-conjugated fusion in DAPQ enhances electron delocalization across the molecule, resulting in improved structural rigidity and stability compared to those of anthraquinone and phenazine alone. After undergoing a two-electron reduction, the half-re-DAPQ enhanced aromaticity in all four rings (A, B, C, and D). In contrast, the fully reduced states of anthraquinone and phenazine (re-Anthraquinone and re-Phenazine) reveal a switch in the aromaticity within their central rings (F and I, respectively). Interestingly, for re-DAPQ, rings A, B, and D retained aromaticity, while ring C became antiaromatic, suggesting an aromaticity exchange between rings B and C during the stepwise reduction. Overall, the π- conjugated fused-ring structure of DAPQ preserves its aromaticity advantages across various redox states, highlighting its robustness as a redox-active material with potential applications in multielectron energy storage.

Electrostatic potential (ESP) energy surface analysis of DAPQ across its reduction states revealed a progressive transition of the four rings from electron-deficient to electron-rich as reduction advanced (Figure 2b).[46] Notably, the relatively uniform distribution of electron density across the rings indicates a high resistance to potential nucleophilic attacks. Furthermore, the highest occupied molecular orbital (HOMO) and lowest unoccupied molecular orbital (LUMO)

https://doi.org/10.1021/jacs.5c17809
J. Am. Chem. Soc. 2025, 147, 46582−46593

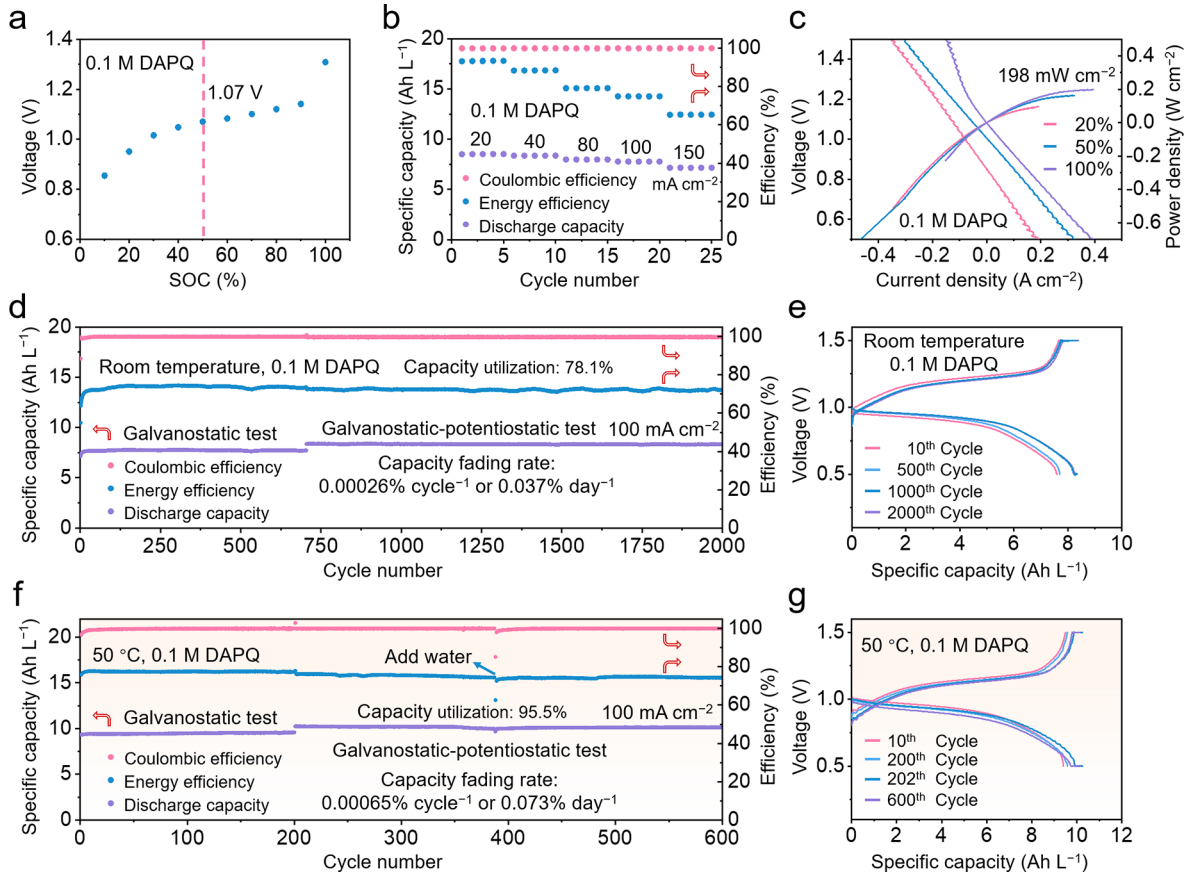

Figure 3. Electrochemical performances of 0.1 M DAPQ||$K_4[Fe(CN)_6]$ AORFBs. (a) The variation of OCVs under different SOCs. (b) Discharge capacity, Coulombic efficiency, and energy efficiency of 0.1 M DAPQ||$K_4[Fe(CN)_6]$ AORFBs evaluated by galvanostatic cycling at various current densities of 20, 40, 80, 100, and 150 mA cm^{-2}, respectively. (c) Polarization and power density curves of 0.1 M DAPQ||$K_4[Fe(CN)_6]$ AORFBs collected at various SOCs of 20%, 50%, and 100%, respectively. (d,f) Cycling performances of 0.1 M DAPQ||$K_4[Fe(CN)_6]$ AORFBs at (d) room temperature and (f) 50 °C. The AORFBs were evaluated upon galvanostatic and subsequent galvanostatic−potentiostatic cycling at a current density of 100 mA cm^{-2} ranging from 0.5 to 1.5 V. (e, g) Charge/discharge curves of 0.1 M DAPQ||$K_4[Fe(CN)_6]$ AORFBs at (e) room temperature and (g) 50 °C.

calculations of anthraquinone, phenazine, and DAPQ (Figures S14, S15, and 2c) revealed that the reduction of carbonyl groups in pristine DAPQ resulted in an energy gap similar to the corresponding anthraquinone derivative.[47−50] However, half-re-DAPQ (1.09 eV) exhibits a much smaller gap than the corresponding phenazine derivative (3.57 eV), indicating that the redox dynamics of the phenazine unit within DAPQ are activated. In its half-reduced state, DAPQ has a higher intrinsic electron transfer rate and better electrochemical kinetics compared with the corresponding phenazine derivative. Additionally, the minimal HOMO energy difference (0.02 eV) between half-re-DAPQ and re-DAPQ suggests that the reduction of carbonyl groups promotes electron transfer among the nitrogen atoms, explaining the closely aligned redox peaks observed during the stepwise reduction.

To evaluate the diffusion coefficients (D) of DHPQ and DAPQ, cyclic voltammetry (CV) measurements of 2 mM DHPQ or DAPQ solutions in 1.0 M KOH were carried out at various scan rates using a glassy carbon (GC) electrode, as shown in Figure S16. Based on the Randles−Sevcik equation, the diffusion coefficients of DHPQ and DAPQ were calculated to be 3.15×10^{-6} cm^2 s^{-1} and 2.41×10^{-6} cm^2 s^{-1}, respectively. The slightly smaller diffusion coefficient of DAPQ is reasonable considering its larger molecular size. Importantly, these values are comparable to those reported for most quinone- and phenazine-based derivatives.[16−18,37,40]

Electrochemical measurements of DHPQ and DAPQ anolytes at a concentration of 0.1 M were comprehensively performed to explore factors affecting their performances. Full AORFBs were assembled using 0.1 M DHPQ or DAPQ solution as the anolyte and an excess amount of $K_4[Fe(CN)_6]$ solution as the catholyte. To further demonstrate the economic viability of AORFBs, custom-made SPEEK membranes (with a production cost of ∼100 $ m^{-2}) were utilized as a cost-effective alternative to commercial Nafion-212 membranes (costing 500−1000 $ m^{-2}).[51,52] The SPEEK membranes were characterized by scanning electron microscopy (SEM), revealing a uniform thickness of 50 μm (Figure S17). The open-circuit voltages (OCVs) of the 0.1 M DAPQ||$K_4[Fe(CN)_6]$ AORFBs were measured as the state of charge (SOC) varied from 10% to 100% (Figure 3a). At 50% SOC, the OCV reached 1.07 V, consistent with the CV results in Figure 1c. In Figures 3b and S18, the rate performances of 0.1 M DAPQ||$K_4[Fe(CN)_6]$ AORFBs are depicted at various current densities (20, 40, 80, 100, and 150 mA cm^{-2}). The energy density and capacity utilization decreased linearly with increasing current density, demonstrating the fixed voltammetric characteristics of the SPEEK membrane. Electrochemical impedance spectroscopy (EIS) analysis indicated

https://doi.org/10.1021/jacs.5c17809
J. Am. Chem. Soc. 2025, 147, 46582−46593

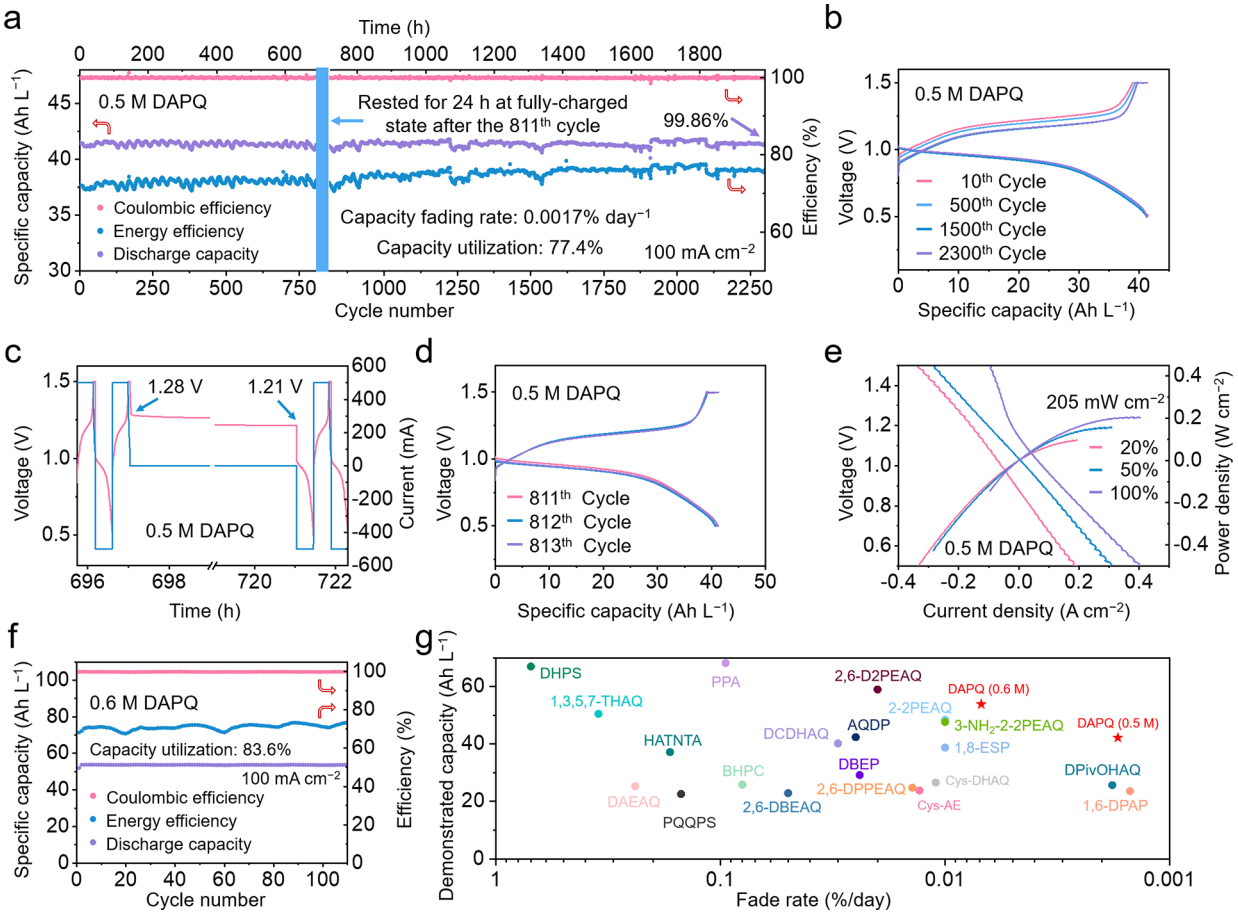

Figure 4. Electrochemical performances of high-concentration DAPQ||$K_4[Fe(CN)_6]$ AORFBs. (a) Long-term galvanostatic−potentiostatic cycling performances of 0.5 M DAPQ||$K_4[Fe(CN)_6]$ AORFBs tested at 100 mA cm^{-2}. (b) Charge/discharge curves of 0.5 M DAPQ||$K_4[Fe(CN)_6]$ AORFBs at the 10th, 500th, 1500th, and 2300th cycles, respectively. (c) Self-discharge test at 100% SOC. The battery was rested for 24 h after being fully charged at the 812th cycle. (d) Corresponding charge/discharge curves from the 811th to the 813th cycle. (e) Polarization and power density curves collected at SOCs of 20%, 50%, and 100%, respectively. (f) Galvanostatic−potentiostatic cycling performances of 0.6 M DAPQ||$K_4[Fe(CN)_6]$ AORFBs tested at 100 mA cm^{-2}. (g) Electrochemical performances of the DAPQ anolyte compared with those of previously reported anthraquinone and phenazine derivatives.

that the resistance of SPEEK membranes exhibited low impedance values (0.43−0.44 Ω cm^2) in 1.0 M KOH solution, 0.1 M DAPQ||$K_4[Fe(CN)_6]$ AORFBs at pH 14 and 0.5 M DAPQ||$K_4[Fe(CN)_6]$ AORFBs at pH 14 (Figure S19). Remarkably, as the current density increases from 20 mA cm^{-2} to 150 mA cm^{-2}, the discharge specific capacity retains 84% of its initial value (from 8.52 Ah L^{-1} to 7.16 Ah L^{-1}), underscoring the excellent rate performance of the DAPQ anolyte. Notably, the four-electron redox-active structure of DAPQ provided it with twice the energy density of conventional anthraquinone or phenazine derivatives at the same concentration. The polarization curves of DAPQ at 20%, 50%, and 100% SOCs were determined at room temperature (Figure 3c). The peak power density of 0.1 M DAPQ||$K_4[Fe(CN)_6]$ AORFBs, measured at 100% SOC, was found to be 198 mW cm^{-2}, demonstrating competitive performance relative to other anthraquinone and phenazine derivatives.[53,54]

To evaluate the capacity decay rates upon different charge/discharge methods, both galvanostatic and galvanostatic−potentiostatic cycling modes were employed, as detailed in the Supporting Information. For the 0.1 M DAPQ||$K_4[Fe(CN)_6]$ AORFBs, the first 700 cycles were conducted using the galvanostatic mode at a current density of 100 mA cm^{-2}, with a charging cutoff voltage of 1.5 V and a discharging cutoff voltage of 0.5 V. The results showed that during the 700 galvanostatic cycles (108.5 h), the maximum specific capacity reached 7.77 Ah L^{-1}, and the final capacity was 7.70 Ah L^{-1}, corresponding to an apparent capacity decay rate of 0.0013% per cycle or 0.20% per day. However, this result was slightly influenced by the ambient temperature fluctuations. To improve accuracy, a galvanostatic−potentiostatic mode was implemented, which can provide a more accurate assessment of the intrinsic stability of the AORFB system. After 1400 galvanostatic−potentiostatic cycles (235 h), the specific capacity decreased marginally from 8.36 Ah L^{-1} to 8.33 Ah L^{-1}, corresponding to a negligible capacity decay rate of 0.00026% per cycle or 0.037% per day (Figure 3d,e). Additionally, although the two pairs of redox peaks of DAPQ exhibit a potential difference of 0.1 V in the CV curves (Figure 1c), only a single, indistinguishable voltage plateau is observed during the charge−discharge process (Figure 3e). Further CV analysis (Figure S20) reveals that the potential separation between the two redox couples of DAPQ is concentration-dependent. As the electrolyte concentration increases, the potential difference between the two redox events gradually decreases. At a concentration of 0.1 M, the DAPQ-based electrolyte displays only one redox peak, indicating that the two relatively independent electron transfer

https://doi.org/10.1021/jacs.5c17809
J. Am. Chem. Soc. 2025, 147, 46582−46593

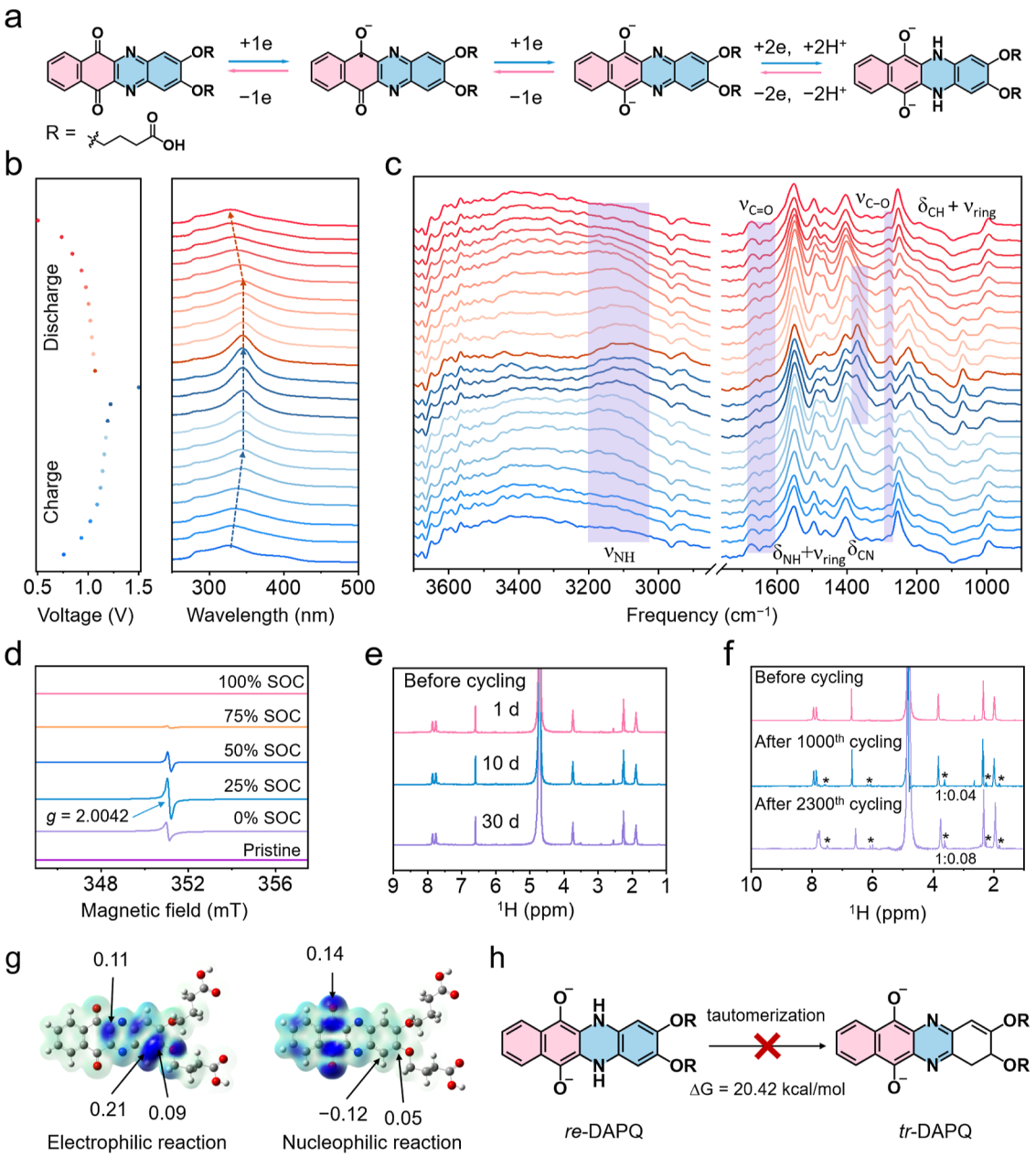

Figure 5. (a) Schematic redox cycles of DAPQ during charge/discharge processes. (b) In situ UV−vis absorption spectra and (c) in situ FTIR spectra of the DAPQ anolyte at various charge/discharge states. (d) EPR spectra of the DAPQ anolyte at different SOCs. (e) Time-dependent ^{1}H NMR spectra of the DAPQ anolyte at pH 14. (f) ^{1}H NMR spectra of DAPQ before and after different cycles. (g) CFF calculations of DAPQ performed by using Gaussian 16 and the MultiWFN 3.8 programs at the DFT B3LYP/6-311 + G(d, p) level. (h) Proposed tautomerization pathway from re-DAPQ to tr-DAPQ.

processes within the DAPQ molecules become increasingly synergistic at higher concentrations.

For comparison, the cycling stability of 0.1 M DHPQ||$K_4[Fe(CN)_6]$ AORFBs was assessed over 1000 cycles under identical conditions (Figure S21). During cycling under galvanostatic mode at 100 mA cm^{-2} after 515 cycles (95 h), the energy efficiency remained at 74.2%, while the discharge specific capacity declined from 9.43 Ah L^{-1} to 9.14 Ah L^{-1}, equating to a capacity decay rate of 0.0061% per cycle or 0.79% per day. In the subsequent 485 galvanostatic−potentiostatic cycles (94 h), the energy efficiency sustained at 74.3%, while the discharge specific capacity decreased from 9.49 Ah L^{-1} to 9.31 Ah L^{-1}, corresponding to a capacity decay rate of 0.0041% per cycle or 0.51% per day. These results highlight that DAPQ demonstrates greatly enhanced cycling stability by an order of magnitude compared to that of the DHPQ intermediate. In addition, ^{1}H NMR analysis of the DHPQ anolyte after 1000 cycles reveals the appearance of several minor impurity peaks (Figure S22), which is consistent with previous reports on hydroxyl-based redox compounds.[19,21] Similarly, the alkoxylation grafting on the DHPQ intermediate significantly enhanced its stability by reducing the electronegativity, thereby mitigating side reactions.

The capability of operating across a wide temperature range is crucial for the broad deployment of AORFBs, particularly in solar-rich regions where elevated operating temperatures are common. Traditional vanadium electrolytes face significant

https://doi.org/10.1021/jacs.5c17809
J. Am. Chem. Soc. 2025, 147, 46582−46593

challenges in a hot climate, as VO_2^+ in the catholyte may precipitate as V_2O_5, compromising stability. Similarly, many organic compounds are susceptible to side reactions at high temperatures. To assess the suitability for high-temperature applications, the DHPQ||$K_4[Fe(CN)_6]$ AORFBs were tested at 50 °C, a temperature representative of environments in solar-intensive regions (Figure 3f,g). The capacity retention after 600 cycles at 50 °C was comparable to that at room temperature, demonstrating the excellent thermal stability and robustness of DAPQ to address challenges posed by elevated temperatures.

Furthermore, the performances of DAPQ||$K_4[Fe(CN)_6]$ AORFBs at a high concentration of 0.5 M were evaluated by using the galvanostatic−potentiostatic cycling mode, which effectively minimizes capacity fluctuations caused by temperature variations and ensures the complete utilization of active materials. As shown in Figure 4a,b, the 0.5 M DAPQ||$K_4[Fe(CN)_6]$ AORFBs, benefiting from a carefully engineered π-conjugated redox core capable of four-electron storage, achieved an impressive energy density of 38.57 Wh L^{-1} (41.47 Ah L^{-1})—twice those of conventional anthraquinone or phenazine derivatives. Furthermore, after an extensive cycling test spanning 2300 cycles (1991 h), the battery retained an energy density of 38.51 Wh L^{-1} (41.41 Ah L^{-1}), with a capacity retention rate of 99.86%. This corresponds to an ultralow capacity fading rate of 0.0017% per day, representing the state-of-the-art performance for alkaline AORFBs operating at high energy densities (Table S1).[16−18,23−31,39,40,44,54−56] Notably, the slight fluctuations observed in Figure 4a arose mainly from external factors (temperature swings or brief power outages) rather than material degradation, further confirming the robustness of the DAPQ molecule.

To further confirm the suitability of DAPQ anolyte for long-term energy storage, a self-discharge test was conducted during the 812th cycle (Figure 4c). Remarkably, after a resting period of 24 h following full charging, the capacity retention remained over 98.72%, and the capacity was fully restored in the subsequent 813th cycle (Figure 4d). This indicates that the observed capacity decay during the resting period was not due to the decomposition of DAPQ but rather attributed to minimal self-discharge behavior within the battery. This result also underscores the high stability of DAPQ in its reduced state, attributed to its rigid π-conjugated structure, which minimizes susceptibility to water-induced nucleophilic degradation. Moreover, while simple analogs of reduced anthraquinone or phenazine derivatives can undergo side reactions, such as disproportionation or intramolecular rearrangement, the distinctive extended conjugation and high molecular rigidity of DAPQ help maintain redox activity and prevent destabilizing electronic or structural reorganizations, thereby contributing to its long-term stability in AORFBs. Additionally, the 0.5 M DAPQ||$K_4[Fe(CN)_6]$ AORFBs exhibited a peak power density of 0.205 W cm^{-2} at 100% SOC (Figure 4e), which is higher than or comparable to those of previously reported phenazine-/anthraquinone-based derivatives in alkaline solutions (Table S1),[16−18,23−31,39,40,44,54−61] thereby demonstrating favorable competitiveness within the field of alkaline redox flow batteries. The rate performances were further evaluated across a range of current densities (50−150 mA cm^{-2}) (Figure S23). Impressively, the high-concentration DAPQ anolyte maintained excellent rate performances, showing energy utilization efficiencies of 85.2%, 77.6%, 73.8%, 70.1%, and 64.7% at current densities of 50, 80, 100, 120, and 150 mA cm^{-2}, respectively. Furthermore, to fully assess the energy density potential of the DAPQ anolyte, the electrochemical performance of nearly saturated DAPQ anolyte (0.6 M) was evaluated (Figures 4f and S24). At a current density of 20 mA cm^{-2}, the 0.6 M DAPQ||$K_4[Fe(CN)_6]$ AORFB achieved an impressive energy density of 53.59 Wh L^{-1} (53.48 Ah L^{-1}). Galvanostatic−potentiostatic tests indicated minimal specific capacity degradation after 110 cycles (130 h) of charge−discharge testing with a reduction from 53.82 Ah L^{-1} to 53.80 Ah L^{-1}. This corresponds to an ultralow capacity fading rate of 0.0069% per day, suggesting exceptional stability of the DAPQ anolyte at high concentrations and rendering it highly advantageous for large-scale energy storage applications. Minor discrepancies in capacity utilization at different concentrations are mainly attributed to temperature fluctuations and other secondary factors but do not affect the evaluation of molecular stability. Additionally, the 0.6 M DAPQ||$K_4[Fe(CN)_6]$ AORFBs exhibited a peak power density of 0.209 W cm^{-2} at 100% SOC (Figure S25). In Figure 4g and Table S1, the electrochemical performances of DAPQ||$K_4[Fe(CN)_6]$ AORFBs were comprehensively compared with prior anthraquinone- or phenazine-based AORFBs, further verifying the exceptional electrochemical performances and stability of DAPQ.[16−18,23−32,40,44,54]

To elucidate the structural changes and potential decomposition mechanisms of DAPQ anolyte during cycling, we conducted a series of in-depth analyses, including in situ UV−vis absorption, in situ FTIR, ex situ EPR, and ex situ NMR spectroscopies. As illustrated in Figure 5a, the redox cycles of DAPQ were proposed based on its redox peaks and by referencing the established redox mechanisms of existing anthraquinone and phenazine derivatives. The charge/discharge processes of the DAPQ anolyte at pH 14 were monitored in real time using in situ UV−vis absorption spectroscopy (Figures 5b and S26). During the charging process, the shoulder peak at λ_{393} nm gradually disappeared, while the main peak at λ_{326} nm underwent a red shift, reaching its maximum value at λ_{345} nm at 50% SOC. This peak continued to intensify as charging progressed, indicating that the redox process of DAPQ proceeds in a stepwise manner. Furthermore, the observed red shift of the absorption peak implies that the reduction of the quinone moiety within the DAPQ molecule reduces the energy barrier for the redox processes of the pyrazine moiety, facilitating smooth electron transfer. This observation aligns well with the computational results presented in Figure 2c.

The structural variations of DAPQ during the charge/discharge processes were further investigated using in situ FTIR spectroscopy (Figures 5c and S27). For the pristine DAPQ anolyte, a stretching vibration of C═O was observed at 1674 cm^{-1}, which disappeared at 50% SOC. Simultaneously, a new absorption peak at 1279 cm^{-1} emerged, corresponding to the reduction of C═O to C−O. Notably, an increase in the intensity of the absorption peak at 3373 cm^{-1} and the emergence of a new peak at 3156 cm^{-1} were also observed. These changes are attributed to the dissociation of the reduced phenolic hydroxyl groups, which form strong hydrogen bonds with solvent water molecules, resulting in the emergence of water molecule vibration peaks. Beyond 50% SOC, the reduction of the pyrazine moiety resulted in the appearance of new peaks at 1371 cm^{-1} (δCN vibration) and 3073 cm^{-1} (νNH), confirming the excellent reversibility of DAPQ during cycling.

https://doi.org/10.1021/jacs.5c17809
J. Am. Chem. Soc. 2025, 147, 46582−46593

Ex situ EPR spectroscopy was employed to monitor the free radical concentration of DAPQ across 0%−100% SOCs (Figure 5d). Although trace radicals remain detectable at 0% SOC due to incomplete redox conversion, no signal was observed in the pristine anolyte before cycling. The free radical concentration peaked at 25% SOC during charging, then dropped, and nearly disappeared by 75% SOC. This observation indicates that, in addition to the stepwise reduction of the quinone and pyrazine moieties, the reduction of the quinone moiety also involves a one-electron transfer and the formation of free radicals. Based on the above analyses, the reduction process of DAPQ primarily involves the following steps: First, the carbonyl group in DAPQ accepts a single electron, forming $DAPQ^{-\bullet}$. As the charging progresses, the carbonyl group is further reduced, and a second one-electron transfer occurs, resulting in $DAPQ^{2-}$.[62] Moreover, $DAPQ^{2-}$ undergoes intermolecular electron transfer with an intact DAPQ molecule, producing $DAPQ^{-\bullet}$. At 50% SOC, nearly all of the carbonyl groups in the DAPQ molecules had been reduced. The subsequent reduction process involves two-electron/two-proton reduction of the pyrazine moiety (Figure 1a). Overall, the redox process of DAPQ is summarized as follows:

From 0% to 50% SOC,

$$DAPQ + e \rightarrow DAPQ^{-\cdot} \quad (1)$$

$$DAPQ^{-\cdot} + e \rightarrow DAPQ^{2-} \quad (2)$$

$$DAPQ + DAPQ^{2-} \rightarrow 2DAPQ^{-\cdot} \quad (3)$$

From 50% to 100% SOC,

$$DAPQ^{2-} + 2e + 2H_2O \rightarrow DAPQ2H^{2-} + 2OH^{-} \quad (4)$$

To further investigate the molecular stability of DAPQ, ex situ NMR spectroscopy was employed to study the anolyte after long-term storage and cycling. As shown in Figures 5e and S28, the ^{1}H NMR and ^{13}C NMR spectra of DAPQ anolyte at pH 14 remained unchanged after being stored for 30 days, confirming the excellent ambient stability of DAPQ. Subsequently, the oxidized and reduced forms of DAPQ anolyte were left to stand for 12 days and characterized by ^{1}H NMR spectroscopy (Figure S29). The results revealed that the hydrolysis of the water-solubilizing groups was effectively suppressed. After long-term cycling tests with different cycle numbers (Figure 5f), the ^{1}H NMR spectra of the retrieved DAPQ anolyte exhibited small new impurity peaks (marked with "*"), which can be attributed to the detachment of the *O*-butanoic acid side chains of DAPQ, leading to the formation of monocarboxylated or decarboxylated DAPQ derivatives. This phenomenon has also been reported in previous studies.[26,28,40] Furthermore, integration of the impurity peak areas revealed that the proportion of hydrolyzed DAPQ molecules in the aliphatic region increased from ∼3.8% after 1000 cycles to ∼7.4% after 2300 cycles. Although the extent of side-chain hydrolysis increases with the number of cycles, it does not compromise the integrity of the redox-active core since the resulting hydrolysis products still exhibit reasonable solubility and stability (Figure S30). Consequently, the electrochemical performance of the AORFB is scarcely affected. It is of particular note that the strict galvanostatic−potentiostatic cycling and rapid charge−discharge tests would strongly accelerate the hydrolysis of the butanoic side chains. In practical applications, however, the side-chain hydrolysis of DAPQ can be substantially alleviated. As illustrated in Figures S31 and S32, no peaks associated with the cleavage of butanoic side chains were detected in the ^{1}H NMR spectrum of a 0.6 M DAPQ electrolyte cycled for 16 days under galvanostatic conditions. These results collectively confirm the exceptional robustness and durability of the quinone−pyrazine redox core as the active center in AORFBs.

The structural stability of the DAPQ molecule was further analyzed by theoretical calculations based on Kenichi Fukui's frontier orbital theory, which identifies electrophilic/nucleophilic reaction sites based on the contributions of HOMO and LUMO orbitals. The condensed Fukui function (CFF) model for electrophilic/nucleophilic reactions was visualized using the MultiWFN 3.8 program (Figure 5g).[48,63] The computational results suggest that the Ar−O−C bond on one side of the DAPQ molecule exhibits a degree of electrophilic reactivity, rendering it slightly prone to hydrolysis and detachment (Figure S30). This is consistent with the ^{1}H NMR observations of the DAPQ anolyte after long-term cycling. Importantly, the peak intensities in ^{1}H NMR spectra indicate that the water-solubilizing group loss due to hydrolysis is minimal and does not compromise the redox stability of the molecule.

To further investigate the possibility of isomerization of the phenazine moiety in DAPQ, DFT calculations were performed to evaluate the tautomerization energy (ΔG) of DAPQ. The ΔG value for the transition from reduced DAPQ (re-DAPQ) to its tautomer (tr-DAPQ) is 20.42 kcal/mol, indicating that re-DAPQ is thermodynamically more favorable (Figure 5h). This stability minimizes the likelihood of isomerization that may disrupt the aromaticity of the redox core, a key factor in maintaining redox reversibility. By integrating theoretical predictions with experimental evidence, it is evident that DAPQ exhibits exceptional molecular stability. The minimal side-chain loss due to hydrolysis, combined with the thermodynamic favorability of its native form, ensures the robust performance of DAPQ during long-term redox cycling.

CONCLUSION

In summary, we report the design and synthesis of a novel water-soluble quinone−pyrazine conjoined π-conjugation derivative DAPQ featuring four charge storage sites, doubling the number in typical quinone or phenazine compounds. Furthermore, the extended fused-ring structure significantly reinforces the electrochemical kinetics and stability, enabling DAPQ to demonstrate impressive rate capability and cycling durability at both room temperature and 50 °C. With four redox sites, DAPQ achieves an impressive electron storage capacity of 2.44 M (65.4 Ah L^{-1}), significantly outperforming most quinone or phenazine derivatives. When coupled with a ferrocyanide catholyte at pH 14, the 0.6 M DAPQ||K_4[Fe(CN)$_6$] AORFBs exhibit an ultrahigh energy density of 53.59 Wh L^{-1} (53.48 Ah L^{-1}) and the 0.5 M DAPQ||K_4[Fe(CN)$_6$] AORFBs showcase exceptional capacity retention at 99.86% after 1991 h of operation (2300 cycles), corresponding to an ultralow capacity decay rate of 0.0017% day^{-1}. These results represent the most exciting level among the currently reported AORFBs. Comprehensive in situ and ex situ spectroscopy techniques, combined with DFT calculations, elucidated the redox mechanism and confirmed the molecular structure stability of DAPQ. These findings highlight the pivotal role of extended molecular conjugation and multiple redox sites in substantially enhancing the energy density and long-term

https://doi.org/10.1021/jacs.5c17809
J. Am. Chem. Soc. 2025, 147, 46582−46593

stability of AORFBs, laying a solid foundation for the ongoing development of AORFBs for scalable, safe, and sustainable energy storage.

■ ASSOCIATED CONTENT

Supporting Information

The Supporting Information is available free of charge at https://pubs.acs.org/doi/10.1021/jacs.5c17809.

Experimental section and additional figures and tables, including FTIR spectra, NMR spectra, UV−vis analyses, CV curves, EIS curves, electrochemical measurements, and battery performance tests (PDF)

■ AUTHOR INFORMATION

Corresponding Author

Zhong Jin − *State Key Laboratory of Coordination Chemistry, MOE Key Laboratory of Mesoscopic Chemistry, MOE Key Laboratory of High Performance Polymer Materials and Technology, Jiangsu Key Laboratory of Advanced Organic Materials, Suzhou Key Laboratory of Green Intelligent Manufacturing of New Energy Materials and Devices, Tianchang New Materials and Energy Technology Research Center, Institute of Green Chemistry and Engineering, School of Sustainable Energy and Resources, School of Chemistry and Chemical Engineering, Nanjing University, Nanjing, Jiangsu 210023, P. R. China;* orcid.org/0000-0001-8860-8579; Email: zhongjin@nju.edu.cn

Authors

Pengbo Zhang − *State Key Laboratory of Coordination Chemistry, MOE Key Laboratory of Mesoscopic Chemistry, MOE Key Laboratory of High Performance Polymer Materials and Technology, Jiangsu Key Laboratory of Advanced Organic Materials, Suzhou Key Laboratory of Green Intelligent Manufacturing of New Energy Materials and Devices, Tianchang New Materials and Energy Technology Research Center, Institute of Green Chemistry and Engineering, School of Sustainable Energy and Resources, School of Chemistry and Chemical Engineering, Nanjing University, Nanjing, Jiangsu 210023, P. R. China*

Yongkang Chen − *State Key Laboratory of Coordination Chemistry, MOE Key Laboratory of Mesoscopic Chemistry, MOE Key Laboratory of High Performance Polymer Materials and Technology, Jiangsu Key Laboratory of Advanced Organic Materials, Suzhou Key Laboratory of Green Intelligent Manufacturing of New Energy Materials and Devices, Tianchang New Materials and Energy Technology Research Center, Institute of Green Chemistry and Engineering, School of Sustainable Energy and Resources, School of Chemistry and Chemical Engineering, Nanjing University, Nanjing, Jiangsu 210023, P. R. China*

Yuzhu Liu − *State Key Laboratory of Coordination Chemistry, MOE Key Laboratory of Mesoscopic Chemistry, MOE Key Laboratory of High Performance Polymer Materials and Technology, Jiangsu Key Laboratory of Advanced Organic Materials, Suzhou Key Laboratory of Green Intelligent Manufacturing of New Energy Materials and Devices, Tianchang New Materials and Energy Technology Research Center, Institute of Green Chemistry and Engineering, School of Sustainable Energy and Resources, School of Chemistry and Chemical Engineering, Nanjing University, Nanjing, Jiangsu 210023, P. R. China*

Jie Wei − *State Key Laboratory of Coordination Chemistry, MOE Key Laboratory of Mesoscopic Chemistry, MOE Key Laboratory of High Performance Polymer Materials and Technology, Jiangsu Key Laboratory of Advanced Organic Materials, Suzhou Key Laboratory of Green Intelligent Manufacturing of New Energy Materials and Devices, Tianchang New Materials and Energy Technology Research Center, Institute of Green Chemistry and Engineering, School of Sustainable Energy and Resources, School of Chemistry and Chemical Engineering, Nanjing University, Nanjing, Jiangsu 210023, P. R. China*

Zuoao Wu − *State Key Laboratory of Coordination Chemistry, MOE Key Laboratory of Mesoscopic Chemistry, MOE Key Laboratory of High Performance Polymer Materials and Technology, Jiangsu Key Laboratory of Advanced Organic Materials, Suzhou Key Laboratory of Green Intelligent Manufacturing of New Energy Materials and Devices, Tianchang New Materials and Energy Technology Research Center, Institute of Green Chemistry and Engineering, School of Sustainable Energy and Resources, School of Chemistry and Chemical Engineering, Nanjing University, Nanjing, Jiangsu 210023, P. R. China*

Binze Yang − *State Key Laboratory of Coordination Chemistry, MOE Key Laboratory of Mesoscopic Chemistry, MOE Key Laboratory of High Performance Polymer Materials and Technology, Jiangsu Key Laboratory of Advanced Organic Materials, Suzhou Key Laboratory of Green Intelligent Manufacturing of New Energy Materials and Devices, Tianchang New Materials and Energy Technology Research Center, Institute of Green Chemistry and Engineering, School of Sustainable Energy and Resources, School of Chemistry and Chemical Engineering, Nanjing University, Nanjing, Jiangsu 210023, P. R. China*

Guochun Ding − *State Key Laboratory of Coordination Chemistry, MOE Key Laboratory of Mesoscopic Chemistry, MOE Key Laboratory of High Performance Polymer Materials and Technology, Jiangsu Key Laboratory of Advanced Organic Materials, Suzhou Key Laboratory of Green Intelligent Manufacturing of New Energy Materials and Devices, Tianchang New Materials and Energy Technology Research Center, Institute of Green Chemistry and Engineering, School of Sustainable Energy and Resources, School of Chemistry and Chemical Engineering, Nanjing University, Nanjing, Jiangsu 210023, P. R. China*

Sheng Wen − *State Key Laboratory of Coordination Chemistry, MOE Key Laboratory of Mesoscopic Chemistry, MOE Key Laboratory of High Performance Polymer Materials and Technology, Jiangsu Key Laboratory of Advanced Organic Materials, Suzhou Key Laboratory of Green Intelligent Manufacturing of New Energy Materials and Devices, Tianchang New Materials and Energy Technology Research Center, Institute of Green Chemistry and Engineering, School of Sustainable Energy and Resources, School of Chemistry and Chemical Engineering, Nanjing University, Nanjing, Jiangsu 210023, P. R. China*

Tengfei Dai − *State Key Laboratory of Coordination Chemistry, MOE Key Laboratory of Mesoscopic Chemistry, MOE Key Laboratory of High Performance Polymer Materials and Technology, Jiangsu Key Laboratory of Advanced Organic Materials, Suzhou Key Laboratory of Green Intelligent Manufacturing of New Energy Materials and Devices, Tianchang New Materials and Energy Technology Research Center, Institute of Green Chemistry*

https://doi.org/10.1021/jacs.5c17809
J. Am. Chem. Soc. 2025, 147, 46582−46593

and Engineering, School of Sustainable Energy and Resources, School of Chemistry and Chemical Engineering, Nanjing University, Nanjing, Jiangsu 210023, P. R. China

Zhihu You − *State Key Laboratory of Coordination Chemistry, MOE Key Laboratory of Mesoscopic Chemistry, MOE Key Laboratory of High Performance Polymer Materials and Technology, Jiangsu Key Laboratory of Advanced Organic Materials, Suzhou Key Laboratory of Green Intelligent Manufacturing of New Energy Materials and Devices, Tianchang New Materials and Energy Technology Research Center, Institute of Green Chemistry and Engineering, School of Sustainable Energy and Resources, School of Chemistry and Chemical Engineering, Nanjing University, Nanjing, Jiangsu 210023, P. R. China*

Zuoxiu Tie − *State Key Laboratory of Coordination Chemistry, MOE Key Laboratory of Mesoscopic Chemistry, MOE Key Laboratory of High Performance Polymer Materials and Technology, Jiangsu Key Laboratory of Advanced Organic Materials, Suzhou Key Laboratory of Green Intelligent Manufacturing of New Energy Materials and Devices, Tianchang New Materials and Energy Technology Research Center, Institute of Green Chemistry and Engineering, School of Sustainable Energy and Resources, School of Chemistry and Chemical Engineering, Nanjing University, Nanjing, Jiangsu 210023, P. R. China*

Yichao Yan − *State Key Laboratory of Coordination Chemistry, MOE Key Laboratory of Mesoscopic Chemistry, MOE Key Laboratory of High Performance Polymer Materials and Technology, Jiangsu Key Laboratory of Advanced Organic Materials, Suzhou Key Laboratory of Green Intelligent Manufacturing of New Energy Materials and Devices, Tianchang New Materials and Energy Technology Research Center, Institute of Green Chemistry and Engineering, School of Sustainable Energy and Resources, School of Chemistry and Chemical Engineering, Nanjing University, Nanjing, Jiangsu 210023, P. R. China*

Complete contact information is available at: https://pubs.acs.org/10.1021/jacs.5c17809

Notes

The authors declare no competing financial interest.

■ ACKNOWLEDGMENTS

This work was supported by the National Natural Science Foundation of China (U25A20628, 22561160129, 22479074, 22475096), the Equipment Pre-Research and Ministry of Education Joint Fund (8091B02052407), the Fundamental Research Program Key Project of Jiangsu Province (BK20253008), the Science and Technology Major Project of Jiangsu Province (BG2024013), the Scientific and Technological Achievements Transformation Special Fund of Jiangsu Province (BA2023037), the Academic Degree and Postgraduate Education Reforming Project of Jiangsu Province (JGKT24_C001), the Key Core Technology Open Competition Project of Suzhou City (SYG2024122), the Open Research Fund of Suzhou Laboratory (SZLAB-1308-2024-TS005), and the Chenzhou National Sustainable Development Agenda Innovation Demonstration Zone Provincial Special Project (2023sfq11).

■ REFERENCES

(1) Simon, P.; Gogotsi, Y. Perspectives for electrochemical capacitors and related devices. *Nat. Mater.* **2020**, *19*, 1151−1163.
(2) Kim, J.; et al. Organic batteries for a greener rechargeable world. *Nat. Rev. Mater.* **2023**, *8*, 54−70.
(3) Zhu, Z.; et al. Rechargeable Batteries for Grid Scale Energy Storage. *Chem. Rev.* **2022**, *122*, 16610−16751.
(4) Bamgbopa, M. O.; Fetyan, A.; Vagin, M.; Adelodun, A. A. Towards eco-friendly redox flow batteries with all bio-sourced cell components. *J. Energy Storage* **2022**, *50*, 104352.
(5) Kebede, A. A.; Kalogiannis, T.; Mierlo, J. V.; Berecibar, M. A comprehensive review of stationary energy storage devices for large scale renewable energy sources grid integration. *Renewable Sustainable Energy Rev.* **2022**, *159*, 112213.
(6) Li, Z.; Jiang, T.; Ali, M.; Wu, C.; Chen, W. Recent Progress in Organic Species for Redox Flow Batteries. *Energy Storage Mater.* **2022**, *50*, 105−138.
(7) Skyllas-Kazacos, M.; Cao, L.; Kazacos, M.; Kausar, N.; Mousa, A. Vanadium Electrolyte Studies for the Vanadium Redox Battery-A Review. *ChemSusChem* **2016**, *9*, 1521−1543.
(8) Lourenssen, K.; Williams, J.; Ahmadpour, F.; Clemmer, R.; Tasnim, S. Vanadium redox flow batteries: A comprehensive review. *J. Energy Storage* **2019**, *25*, 100844.
(9) Huskinson, B.; et al. A metal-free organic-inorganic aqueous flow battery. *Nature* **2014**, *505*, 195−198.
(10) Yang, G.; et al. Organic Electroactive Materials for Aqueous Redox Flow Batteries. *Adv. Mater.* **2023**, *35* (33), No. e2301898.
(11) Luo, J.; Hu, B.; Hu, M.; Zhao, Y.; Liu, T. L. Status and Prospects of Organic Redox Flow Batteries toward Sustainable Energy Storage. *ACS Energy Lett.* **2019**, *4*, 2220−2240.
(12) Poizot, P.; et al. Opportunities and Challenges for Organic Electrodes in Electrochemical Energy Storage. *Chem. Rev.* **2020**, *120*, 6490−6557.
(13) Pan, M.; et al. Reversible Redox Chemistry in Pyrrolidinium-Based TEMPO Radical and Extended Viologen for High-Voltage and Long-Life Aqueous Redox Flow Batteries. *Adv. Energy Mater.* **2022**, *12*, 2103478.
(14) DeBruler, C.; et al. Designer Two-Electron Storage Viologen Anolyte Materials for Neutral Aqueous Organic Redox Flow Batteries. *Chem* **2017**, *3*, 961−978.
(15) Ding, Y.; Yu, G. The Promise of Environmentally Benign Redox Flow Batteries by Molecular Engineering. *Angew. Chem., Int. Ed. Engl.* **2017**, *56*, 8614−8616.
(16) Wang, C.; Yu, B.; Liu, Y.; Wang, H.; Zhang, Z.; Xie, C.; Li, X.; Zhang, H.; Jin, Z. N-alkyl-carboxylate-functionalized anthraquinone for long-cycling aqueous redox flow batteries. *Energy Storage Mater.* **2021**, *36*, 417−426.
(17) Wang, C.; et al. Molecular Design of Fused-Ring Phenazine Derivatives for Long-Cycling Alkaline Redox Flow Batteries. *ACS Energy Lett.* **2020**, *5*, 411−417.
(18) Pang, S.; Wang, X.; Wang, P.; Ji, Y. Biomimetic Amino Acid Functionalized Phenazine FlowBatteries with Long Lifetime at Near-Neutral pH. *Angew. Chem., Int. Ed.* **2021**, *60*, 5349−5358.
(19) Huang, S.; et al. Molecular engineering of dihydroxyanthraquinone-based electrolytes for high-capacity aqueous organic redox flow batteries. *Nat. Commun.* **2022**, *13*, 4746.
(20) Jing, Y.; et al. In-situ electrochemical recomposition of decomposed redox-active species in aqueous organic flow batteries. *Nat. Chem.* **2022**, *14*, 1103−1109.
(21) Fontmorin, J.-M.; Guiheneuf, S.; Godet-Bar, T.; Floner, D.; Geneste, F. How anthraquinones can enable aqueous organic redox flow batteries to meet the needs of industrialization. *Curr. Opin. Colloid Interface Sci.* **2022**, *61*, 101624.
(22) Zhang, L.; Feng, R.; Wang, W.; Yu, G. Emerging chemistries and molecular designs for flow batteries. *Nat. Rev. Chem.* **2022**, *6*, 524−543.
(23) Hu, B.; Li, H.; Fan, H.; Song, J. A long-lifetime aqueous organic redox flow battery utilizing multi-redox anolyte. *Energy Storage Mater.* **2023**, *59*, 102789.

(24) Lin, K.; et al. Alkaline quinone flow battery. *Science* **2015**, *349*, 1529−1532.
(25) Wu, M.; et al. Extremely Stable Anthraquinone Negolytes Synthesized from Common Precursors. *Chem* **2020**, *6*, 1432−1442.
(26) Kwabi, D. G.; et al. Alkaline Quinone Flow Battery with Long Lifetime at pH 12. *Joule* **2018**, *2*, 1894−1906.
(27) Amini, K.; et al. An Extremely Stable, Highly Soluble Monosubstituted Anthraquinone for Aqueous Redox Flow Batteries. *Adv. Funct. Mater.* **2023**, *33*, 2211338.
(28) Ji, Y.; et al. A Phosphonate-Functionalized Quinone Redox Flow Battery at Near-Neutral pH with Record Capacity Retention Rate. *Adv. Energy Mater.* **2019**, *9*, 1900039.
(29) Jin, S.; et al. A Water-Miscible Quinone Flow Battery with High Volumetric Capacity and Energy Density. *ACS Energy Lett.* **2019**, *4*, 1342−1348.
(30) Guiheneuf, S.; et al. A new hydroxyanthraquinone derivative with a low and reversible capacity fading process as negolyte in alkaline aqueous redox flow batteries. *J. Power Sources* **2022**, *539*, 231600.
(31) Wu, M.; Bahari, M.; Fell, E. M.; Gordon, R. G.; Aziz, M. J. High-performance anthraquinone with potentially low cost for aqueous redox flow batteries. *J. Mater. Chem. A* **2021**, *9*, 26709−26716.
(32) Xu, J.; Pang, S.; Wang, X.; Wang, P.; Ji, Y. Ultrastable aqueous phenazine flow batteries with high capacity operated at elevated temperatures. *Joule* **2021**, *5*, 2437−2449.
(33) Tuttle, M. R.; Davis, S. T.; Zhang, S. Synergistic Effect of Hydrogen Bonding and $\pi-\pi$ Stacking Enables Long Cycle Life in Organic Electrode Materials. *ACS Energy Lett.* **2021**, *6*, 643−649.
(34) Chen, Y.; et al. Two-Dimensional Organic Supramolecule via Hydrogen Bonding and $\pi-\pi$ Stacking for Ultrahigh Capacity and Long-Life Aqueous Zinc−Organic Batteries. *Angew. Chem., Int. Ed. Engl.* **2022**, *134*, No. e202116289.
(35) Shi, Y.; et al. π-Conjugated N-heterocyclic compound with redox-active quinone and pyrazine moieties as a high-capacity organic cathode for aqueous zinc-ion batteries. *Chem. Eng. J.* **2023**, *461*, 141850.
(36) Romadina, E. I.; Komarov, D. S.; Stevenson, K. J.; Troshin, P. A. New phenazine based anolyte material for high voltage organic redox flow batteries. *Chem. Commun.* **2021**, *57*, 2986−2989.
(37) Lin, Z.; et al. A high capacity small molecule quinone cathode for rechargeable aqueous zinc-organic batteries. *Nat. Commun.* **2021**, *12*, 4424.
(38) Gu, P.-Y.; et al. Synthesis, physical properties, and light-emitting diode performance of phenazine-based derivatives with three, five, and nine fused six-membered rings. *J. Org. Chem.* **2015**, *80*, 3030−3035.
(39) Hollas, A.; et al. A biomimetic high-capacity phenazine-based anolyte for aqueous organic redox flow batteries. *Nat. Energy* **2018**, *3*, 508−514.
(40) Liu, Y.; et al. Screening Ultra-Stable (Phenazine)dioxyalkanocic Acids with Varied Water-Solubilizing Chain Lengths for High-Capacity Aqueous Redox Flow Batteries. *J. Am. Chem. Soc.* **2024**, *146*, 3293−3302.
(41) Kong, T.; et al. Enabling Long-Life Aqueous Organic Redox Flow Batteries with a Highly Stable, Low Redox Potential Phenazine Anolyte. *ACS Appl. Mater. Interfaces* **2024**, *16*, 752−760.
(42) Kwabi, D. G.; Ji, Y.; Aziz, M. J. Electrolyte Lifetime in Aqueous Organic Redox Flow Batteries: A Critical Review. *Chem. Rev.* **2020**, *120*, 6467−6489.
(43) Briot, L.; Petit, M.; Cacciuttolo, Q.; Pera, M.-C. Aging phenomena and their modelling in aqueous organic redox flow batteries: A review. *J. Power Sources* **2022**, *536*, 231427.
(44) Wang, C.; et al. Alkaline soluble 1,3,5,7-tetrahydroxyanthraquinone with high reversibility as anolyte for aqueous redox flow battery. *J. Power Sources* **2022**, *524*, 231001.
(45) Geuenich, D.; Hess, K.; Köhler, F.; Herges, R. Anisotropy of the Induced Current Density (ACID), a General Method To Quantify and Visualize Electronic Delocalization. *Chem. Rev.* **2005**, *105*, 3758−3772.
(46) Lu, T.; Chen, F. Multiwfn A multifunctional wavefunction analyzer. *J. Comput. Chem.* **2012**, *33*, 580−592.
(47) Stratmann, R. E.; Burant, J. C.; Scuseria, G. E.; Frisch, M. J. Improving harmonic vibrational frequencies calculations in density functional theory. *J. Chem. Phys.* **1997**, *106*, 10175−10183.
(48) Hohenberg, P.; Kohn, W. Inhomogeneous electron gas. *Phys. Rev. B* **1964**, *136*, B864−B871.
(49) Perdew, J. P.; Wang, Y. Accurate and simple analytic representation of the electron-gas correlation energy. *Phys. Rev. B* **1992**, *45*, 13244−13249.
(50) Krishnan, R.; Binkley, J. S.; Seeger, R. J.; Pople, A. Self-consistent molecular orbital methods. XX. A basis set for correlated wave functions. *J. Chem. Phys.* **1980**, *72*, 650−654.
(51) Winardi, S.; et al. Sulfonated poly (ether ether ketone)-based proton exchange membranes for vanadium redox battery applications. *J. Membr. Sci.* **2014**, *450*, 313−322.
(52) Yuan, Z.; et al. Low-cost hydrocarbon membrane enables commercial-scale flow batteries for long-duration energy storage. *Joule* **2022**, *6*, 884−905.
(53) Liu, Y.; et al. Organic electrolytes for aqueous organic flow batteries. *Mater. Today Energy* **2021**, *20*, 100634.
(54) Jing, Y.; et al. Anthraquinone Flow Battery Reactants with Nonhydrolyzable Water-Solubilizing Chains Introduced via a Generic Cross-Coupling Method. *ACS Energy Lett.* **2022**, *7*, 226−235.
(55) Liu, Y.; et al. Artificial α-amino acid based on cysteine grafted natural aloe-emodin for aqueous organic redox flow batteries. *Nat. Commun.* **2025**, *16*, 2965.
(56) Zhang, P.; et al. An amphoteric and hydrogen-bond-rich artificial α-amino acid for highly durable aqueous redox flow batteries. *Nat. Commun.* **2025**, *16*, 4727.
(57) Kerr, E. F.; et al. High Energy Density Aqueous Flow Battery Utilizing Extremely Stable, Branching-Induced High-Solubility Anthraquinone near Neutral pH. *ACS Energy Lett.* **2023**, *8*, 600−607.
(58) Alfaraidi, A. M.; et al. An Extremely Stable and Soluble NH_2-Substituted Anthraquinone Electrolyte for Aqueous Redox Flow Batteries. *ACS Appl. Energy Mater.* **2023**, *6*, 12259−12266.
(59) Pang, S.; et al. A phenazine-based high-capacity and high-stability electrochemical CO2 capture cell with coupled electricity storage. *Nat. Energy* **2023**, *8*, 1126−1136.
(60) Zhang, X.; Li, L.; Ji, Y.; Wang, P. A Six-Electron Energy Storage Material for Ultra-Stable Aqueous Organic Redox Flow Batteries. *Adv. Sci.* **2025**, No. e14452.
(61) Ding, G.; et al. π-Conjugation extended phenazinization of natural prosthetic group pyrroloquinoline quinone disodium salt for long-lifespan biomimetic aqueous redox flow batteries. *Nano Energy* **2025**, *144*, 111404.
(62) Zhao, E. W.; et al. Coupled In-situ NMR and EPR Studies Reveal the Electron Transfer Rate and Electrolyte Decomposition in Redox Flow Batteries. *J. Am. Chem. Soc.* **2021**, *143*, 1885−1895.
(63) Rong, F.; Tian, L.; Fei-Wu, C. Comparing Methods for Predicting the Reactive Site of Electrophilic Substitution. *Acta Phys.-Chim. Sin.* **2014**, *30*, 628−639.

https://doi.org/10.1021/jacs.5c17809
J. Am. Chem. Soc. 2025, 147, 46582−46593